Journal of Power Sources 388 (2018) 57–64

Contents lists available at ScienceDirect

Journal of Power Sources

journal homepage: www.elsevier.com/locate/jpowsour

# $Na_{1.25}Ni_{1.25}Fe_{1.75}(PO_4)_3$ nanoparticles as a janus electrode material for Li-ion batteries

Claude Karegeya[a,b], Abdelfattah Mahmoud[a,*], Frédéric Hatert[c], Bénédicte Vertruyen[a], Rudi Cloots[a], Pierre-Emmanuel Lippens[d], Frédéric Boschini[a]

[a] GREENMAT, CESAM, Institute of Chemistry B6, University of Liège, 4000, Liège, Belgium
[b] Faculty of Sciences, College of Education, University of Rwanda, 5039, Kigali, Rwanda
[c] Laboratory of Mineralogy B18, University of Liège, 4000, Liège, Belgium
[d] Institut Charles Gerhardt, UMR 5253 CNRS, Université de Montpellier, Place Eugène Bataillon, 34095, Montpellier Cedex 5, France

## HIGHLIGHTS

- $Na_{1.25}Ni_{1.25}Fe_{1.75}(PO_4)_3$ material was prepared by solvothermal method.
- Ethylene glycol limits $Na_{1.25}Ni_{1.25}Fe_{1.75}(PO_4)_3$ particles agglomeration.
- Vacancies in $Na_{1.25}Ni_{1.25}Fe_{1.75}(PO_4)_3$ enhance the electrochemical performance.
- $Na_{1.25}Ni_{1.25}Fe_{1.75}(PO_4)_3$ shows excellent dual electrochemical performance.

## GRAPHICAL ABSTRACT

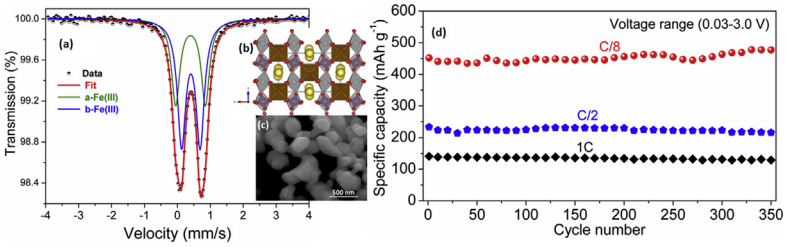


## ARTICLE INFO

*Keywords:*
$Na_{1.25}Ni_{1.25}Fe_{1.75}(PO_4)_3$
Solvothermal synthesis
Nanoparticles
Dual electrode material
Insertion and conversion reaction
Lithium-ion battery

## ABSTRACT

A solvothermal method was used to prepare $Na_{1.25}Ni_{1.25}Fe_{1.75}(PO_4)_3$ nanoparticles, a new promising electrode material for lithium-ion batteries. The composition and the crystal structure were determined by $^{57}$Fe Mössbauer spectroscopy and powder X-ray diffraction Rietveld refinements and confirmed by magnetic measurements. The structural formula $\square_{0.75}Na_{1.25}Ni_{1.25}Fe_{1.75}(PO_4)_3$ was obtained showing a significant amount of Na vacancies, which enhances Li diffusion. $Na_{1.25}Ni_{1.25}Fe_{1.75}(PO_4)_3$ was used as negative and positive electrode material and shows excellent electrochemical performances. As negative electrode in the voltage range 0.03-3.5 V vs. $Li^+$/Li, the first discharge at current density of 40 mA $g^{-1}$ delivers a specific capacity of 1186 mAh $g^{-1}$, which is almost three times its theoretical capacity (428 mAh $g^{-1}$). Then, reversible capacity of 550 mAh $g^{-1}$ was obtained at 50 mA $g^{-1}$ with high rate capability (150 mAh $g^{-1}$ at 500 mA $g^{-1}$) and capacity retention of 350 cycles. As positive electrode material, specific capacities of about 145 and 99 mAh $g^{-1}$ were delivered at current densities of 5 and 50 mA $g^{-1}$, respectively, in the voltage range of 1.5–4.5 V *vs.* $Li^+$/Li. In addition, we show that the use of solvothermal synthesis contributes to the synthesis of small sized particles leading to good electrochemical performances.

## 1. Introduction

Iron-phosphate-based materials have been largely investigated as positive electrodes of lithium-ion and sodium-ion batteries. Currently their use as negative electrode materials has also got more attention. They offer many advantages over other electrode materials due to the fact that they are environmental friendly, non toxic with high rate capability [1]. Although they are mainly produced by solid-state

* Corresponding author. Tel.: +32 (0)4 366 3543; fax: +32 (0)4 366 3413.
*E-mail addresses:* abdelfattah.mahmoud@ulg.ac.be, mahmoudrca@gmail.com (A. Mahmoud).

https://doi.org/10.1016/j.jpowsour.2018.03.069
Received 1 January 2018; Received in revised form 14 March 2018; Accepted 26 March 2018
Available online 02 April 2018
0378-7753/ 

synthesis route, the exploration of various synthesis techniques has shown that wet chemistry approaches produce suitable powder morphology with smaller particle size [2].

Nanoparticles receive great interest in various applications including catalysts, medicine, chemical sensors, energy conversion, energy storage systems, and many other fields [3–7]. They are mainly prepared through solution chemistry methods. These routes are known as efficient methods to produce nanomaterials with excellent properties that can be obtained by simply optimizing synthetic conditions. The particle size reduction is one of the main strategies employed to improve the performance of electrode materials, for example during the hydro/solvothermal process [8]. In this context, researchers have increased their efforts in developing multiple approaches to design and prepare nanoparticles with various morphologies. This leads to the nanosized materials with enhanced physical/chemical properties for specific applications. Among various synthetic methods, the wet chemical preparation routes, such as hydrothermal/solvothermal [9–15], microwave hydrothermal [16], sol–gel [17,18] or co-precipitation [19,20] methods, offer an indisputable advantage in achieving better homogeneity and mixing of the precursors material to produce electrode materials with high crystallinity, high purity, and small particle size distribution [21–23]. For applications as energy storage systems, nanoparticles are especially attractive due to their high specific area in boosting the electrochemical performance. In this regard, we report here a surfactant-free solvothermal preparation followed by heat treatment to obtain nanoparticles of $Na_{1.25}Ni_{1.25}Fe_{1.75}(PO_4)_3$ called NNFP in the present paper. The study of nickel-iron phosphate-based compound as dual electrode materials was reported for the first time in 2015 by Essehli et al. [24], who published the crystallographic, magnetic and electrochemical characterization of α-$Na_2Ni_2Fe(PO_4)_3$ materials obtained by solid state synthesis. The solvothermal method used in the present work is more suitable to obtain nanostructured material with expected higher electrochemical performances, especially in terms of rate capability. In addition, the composition of our isostructural $\square_{0.75}Na_{1.25}Ni_{1.25}Fe_{1.75}(PO_4)_3$ material provides more vacant sites for $Li^+$ or $Na^+$ insertion. This technique was previously used to prepare uniform $LiFePO_4$ nanoplates in ethylene glycol as solvent and the nanoparticles obtained through this synthesis method displayed good electrochemical properties as electrode material for Li-ion batteries [25,26]. This method was modified here to obtain NNFP nanoparticles displaying excellent electrochemical performances. The use of ethylene glycol unexpectedly induced the formation of a gel-like intermediate, resulting in NNFP nanoparticles formation after heat treatment, which can be considered as new electrode family for lithium and sodium-ion batteries.

We report here the first electrochemical tests of NNFP as electrode material for Li-ion batteries. The main advantages of this material are dual electrochemical properties (as positive and negative electrodes), high electrochemical performance, abundant raw material resources, low cost, environmental compatibility, remarkable thermal stability, high safety and relatively high theoretical specific capacities.

## 2. Experimental section

### 2.1. Synthesis of nanostructured $Na_{1.25}Ni_{1.25}Fe_{1.75}(PO_4)_3$

In a typical procedure, 6 mmol $NH_4H_2PO_4$ (≥99%, Acros), 2.5 mmol $Ni(NO_3)_2.6H_2O$ (99%, Merck), 3.5 mmol $Fe(NO_3)_3.6H_2O$ (96%, Riedel-de Haën), and 8 mmol $NaNO_3$ (99.999%, Sigma Aldrich) were dissolved in 60 ml of ethylene glycol under vigorous stirring. The mixture was stirred for 15 min to obtain an homogeneous blue solution and then transferred into a 125 ml Teflon cup. The teflon-lined stainless-steel autoclave was sealed under air and heated at 180 °C for 6 h in an electric oven. After cooling to room temperature, the precipitate was collected and washed with absolute ethanol and distilled water several times. The as-obtained sol-gel product was then dried at 80 °C for 2 h in a vacuum oven and finally heated in a furnace at 550 °C for 10 h in air atmosphere.

### 2.2. Characterizations

Powder X-ray diffraction (XRD) data were collected with a Bruker D8 ECO powder diffractometer using Cu Kα radiation (λ = 1.5418 Å), operating from 2θ = 2–100°. The crystal structure was refined by the Rietveld method, starting from the observed powder diffraction pattern and using the TOPAS software [27]. The morphology and particle size of NNFP were studied with a scanning electron microscope (XL 30 FEG-ESEM, FEI). Measurements of specific surface area and texture properties which includes analysis of porosity for NNFP sample were determined through measuring Nitrogen ($N_2$) sorption isotherms at 77 K with Micrometric ASAP2020 system.

$^{57}$Fe transmission Mössbauer spectroscopy data were recorded by using a constant-acceleration spectrometer with a $^{57}$Co(Rh) source at room temperature. The Mössbauer absorbers were prepared with about 30 mg of NNFP mixed with boron nitride. The spectrometer was calibrated at room temperature with the magnetically split sextet spectrum of a high-purity α-Fe foil as the reference absorber. The measurements were carried out in the velocity range ± 4 mm/s with optimal energy resolution. The Mössbauer spectra were fitted using Lorentzian doublets using the Fullham program [28]. In this way, the isomer shift (δ), the quadrupole splitting (Δ), the linewidth (Γ) and the relative resonance areas of the different spectral components were determined.

The magnetic susceptibility of NNFP, χ, was measured with a Superconducting Quantum Interference Design (SQUID) magnetometer MPMS XL7. The sample was cooled to 2 K under a zero magnetic field (ZFC). Then, a magnetic field of 100 mT was applied, and the susceptibility was recorded from 2 to 300 K.

Electrochemical measurements were conducted in two-electrode Swagelok cells, using Li metal (Aldrich) as anode material which also operated as a reference electrode, and 1 M $LiPF_6$ in ethylene carbonate/dimethylcarbonate (1/1, v/v) as electrolyte solution. NNFP active material (60%wt) was mixed with carbon black (CB, 20%wt) and polyvinylidene fluoride (PVDF, 20%wt) and then ground together for 30 min. Pellets with 13 mm diameter were prepared by uniaxial pressing on a stainless steel grid. The current collectors were stainless steel and the separator between electrodes was a 25 µm monolayer polypropylene membrane. All the assembly processes for the Swagelok cells were conducted in an argon filled glove box. The charge/discharge curves were performed in galvanostatic mode with different potential windows for NNFP as negative electrode: 0.03–3.5 V *vs.* $Li^+/Li^0$ and as positive electrode: 1.5–4.5 V *vs.* $Li^+/Li^0$ using the Neware Electrochemical Test System. The initial step for NNFP as anode is a discharge ending at 0.03 V while that of NNFP as cathode is a charge ending at 4.5 V.

For the study of NNFP as electrode material for sodium-ion batteries. the electrode preparation was performed in similar conditions as for lithium-ion batteries tests using Na as the counter/reference electrode, the Whatman separator soaked in $NaPF_6$ in PC with 5% FEC electrolyte.

## 3. Results and discussions

### 3.1. $^{57}$Fe Mössbauer spectroscopy

The $^{57}$Fe Mössbauer spectrum of NNFP, measured at room temperature, is formed by two peaks that can be fitted to two doublets (Fig. 1). The hyperfine Mössbauer parameters are reported in Table 1 for the two types of iron atoms labelled a-Fe and b-Fe. The small values of the full width at half-maximum (Γ) confirm the existence of only two types of Fe environments. The close values of the isomer shift ($\approx 0.4$ mm s$^{-1}$) for a-Fe and b-Fe are typical of high spin Fe(III) oxidation state in $FeO_6$ octahedral environments [25]. The absence of

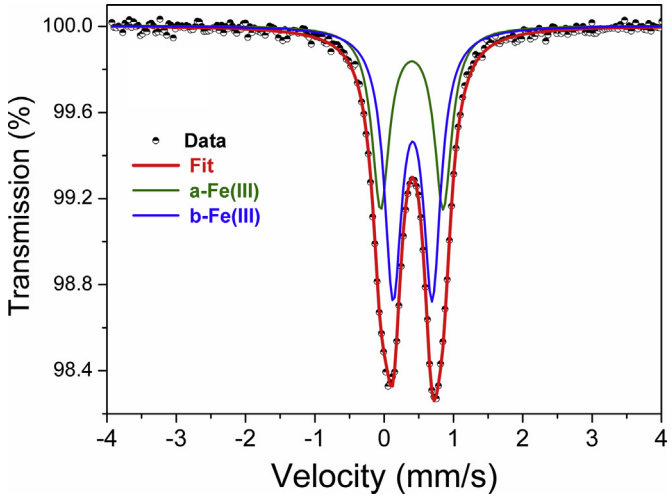


**Fig. 1.** $^{57}$Fe Mossbauer spectrum recorded at room temperature for $Na_{1.25}Ni_{1.25}Fe_{1.75}(PO_4)_3$.

**Table 1**
Fitted Mössbauer parameters[a] of $Na_{1.25}Ni_{1.25}Fe_{1.75}(PO_4)_3$ sample recorded at room temperature.

| | δ (mm s$^{-1}$) | Δ (mm s$^{-1}$) | Γ (mm s$^{-1}$) | Area (%) |
|---|---|---|---|---|
| a-Fe(III) | 0.40 (1) | 0.90 (4) | 0.30 (2) | 41 (1) |
| b-Fe(III) | 0.41 (1) | 0.56 (3) | 0.30 (1) | 59 (1) |

[a] δ-Isomer shift, referred to α-iron at 295 K, Δ-quadrupole splitting, Γ-line width.

hyperfine magnetic splitting indicates that NNFP is paramagnetic at room temperature and there are no magnetic impurities such as iron oxides at the 1 Fe-at% level. The values of the quadrupole splitting Δ(a-Fe) = 0.9 mm s$^{-1}$ and Δ(b-Fe) = 0.56 mm s$^{-1}$ show that the environment of a-Fe is more distorted than that of b-Fe. Our values of the Mössbauer parameters are close to those previously found for α-$Na_2Ni_2Fe(PO_4)_3$ [24] but the ratio a-Fe/b-Fe = 0.72, obtained here by considering the same recoilless fraction f(a-Fe) = f(b-Fe), strongly differs from that obtained for α-$Na_2Ni_2Fe(PO_4)_3$ (0.92), indicating a different distribution of the Fe atoms among the crystallographic sites.

### 3.2. Crystallographic characterization

The crystal structure of NNFP was refined with the Rietveld method by considering the structure of α-$Na_2Ni_2Fe(PO_4)_3$ as a starting model [24]. A good agreement between the experimental data and the Rietveld refinement was obtained as shown in Fig. 2a and by the values of the reliability factors (Table 2). The orthorhombic space group *Imma* was confirmed and the lattice parameters reported in Table 2 are close to those obtained previously [24]. However, there are some differences in the coordinates and the occupation of the atomic sites (Table 3), leading to significantly different chemical composition from that obtained by these authors. This aspect is crucial for the electrochemical mechanism (number of vacant sites and Fe/Ni ratio) and a particular attention was paid to the accurate determination of the site occupation by considering the following approach.

There are two possible crystallographic sites with 4a and 8g symmetries for the transition metals. In the refinement procedure, the Ni/Fe ratios were constrained for these two sites because Ni and Fe cannot be distinguished by XRD due to their similar X-ray scattering factors. Regardless of the metal occupation, the amount and the repartition of Na on the 4b and 4e sites were obtained leading to 1.27(4) Na per formula unit (f.u.) with approximatively the same occupations for these two sites (Table 3). The relative amounts of Fe and Ni were then evaluated by considering the charge neutrality of the compound, giving 1.73 Fe(III) + 1.27 Ni(II) per f.u. For the Fe occupation of the 4e and 8g sites, we considered the Mössbauer results: b-Fe should occupy the less distorted sites and represent 59% of the Fe atoms, which corresponds to 1 Fe per f.u. In addition, the effective ionic radius of Fe(III) in octahedral coordination (0.645 Å) [29] is smaller than that of Ni(II) (0.690 Å), which means that the larger Fe (III)-content should be on the smaller and less distorted site 4e (Table 4). Thus, these sites are fully occupied by b-Fe. The remaining 0.73 Fe per f.u, that exactly correspond to the 41% of a-Fe evaluated by Mössbauer spectroscopy, occupy 36% of the 8g sites and the Ni atoms occupy the remaining 64% of the 8g sites.

Thus, the structural formula of our compound, obtained by combining Mössbauer and XRD experiments is $(Na_{0.62}\square_{0.38})_{4e}(Na_{0.66}\square_{0.34})_{4b}(Fe_{0.72}Ni_{1.28})_{8g}(Fe_{1.00})_{4a}(PO_4)_3$, leading to the chemical composition $\square_{0.72}Na_{1.28}Ni_{1.28}Fe_{1.72}(PO_4)_3$. Finally, the calculated interatomic distances are consistent with the existence of high-spin Fe(III) and Ni(II) in oxygen based octahedral environments and of P(V) in $PO_4$ tetrahedra (Table 4).

### 3.3. Crystal structure

$Na_{1.25}Ni_{1.25}Fe_{1.75}(PO_4)_3$ is isostructural to α-$Na_2Ni_2Fe(PO_4)_3$, $Na\square V_3(PO_4)_3$ and $Sr\square Fe_3(PO_4)_3$ (□: vacancy), which crystallize with a stuffed α-$CrPO_4$ type structure [24,30–32]. The basic structural unit is a $[M_2O_{10}]$ dimer (M = Ni1, Fe1 at 8g) constituted by two edge-sharing octahedra, connected in the *c* direction by corner-sharing $PO_4$ tetrahedra (Fig. 2b). These connected dimers form planes perpendicular to the *a* axis, between which occur the $FeO_6$ octahedra (Fe2 at 4e) (Fig. 2c and d). These $FeO_6$ octahedra are connected together by corner-sharing $PO_4$ tetrahedra, to form chains parallel to the *b* axis (Fig. 2b). As shown in Fig. 2c, Na atoms occur in large channels, parallel to the *b* crystallographic axis. Due to the composition $Na_{1.25}Ni_{1.25}Fe_{1.75}(PO_4)_3$ the sites are partially occupied within the channels, enhancing ionic diffusion.

### 3.4. Magnetic measurements

The inverse magnetic susceptibility of NNFP follows a Curie Weiss law above about 100 K (Fig. 3). The experimental data were linearly fitted in the range 200–300 K. The Curie temperature θ = −107 K indicates strong antiferromagnetic spin interactions, while the Curie constant C = 8.64 emu.K.mol$^{-1}$ per f.u gives the effective magnetic moment $\mu_{eff}$ = 8.3 $\mu_B$. The latter value is in excellent agreement with the spin-only value evaluated for 1.25 Ni(II) and 1.75 high-spin Fe(III): $\mu_{eff}$ = 8.4 $\mu_B$. The magnetic moment of our compound is significantly higher than the previously obtained one: $\mu_{eff}$ = 7.14 $\mu_B$ obtained for α-$Na_2Ni_2Fe(PO_4)_3$ [24], which confirms the present composition of NNFP determined by combining Mössbauer spectroscopy and XRD.

### 3.5. Particle morphology, specific surface area and porosity

The morphology and the nanostructure of NNFP were investigated by scanning electron microscopy (SEM) and transmission electron microscopy (TEM) as shown in Fig. 4. Fig. 4a and b shows the SEM images of NNFP under different magnifications. The low magnification SEM image (Fig. 4a) reveals that NNFP nanoparticles are agglomerated together with a rather uniform size distribution. The high magnification image (Fig. 4b) shows that the particle sizes are in the range 200–500 nm. Thus, the NNFP nanoparticles provide a large surface area, improving the electrolyte impregnation. Such a feature is of high importance for electrode materials since it facilitates the insertion/deinsertion of $Na^+/Li^+$ ions within the material and reduces the electrode polarization. The TEM image (Fig. 4c) confirms the small size of the NNFP particles.

Nitrogen ($N_2$) adsorption–desorption isotherms were collected to study the specific surface area and porosity of the studied sample

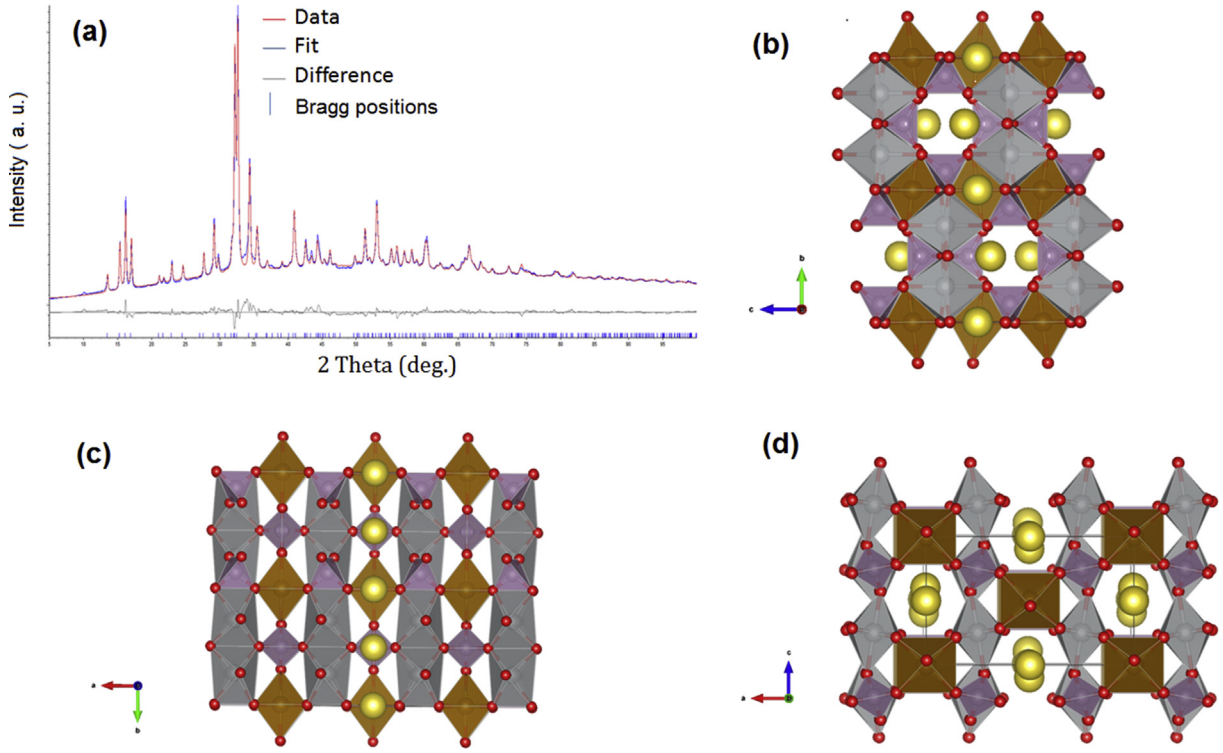


**Fig. 2.** a) Final observed, calculated, and difference plots for XRPD (Cu Kα radiation) refinement of $Na_{1.25}Ni_{1.25}Fe_{1.75}(PO_4)_3$. b) The crystal structure of $Na_{1.25}Ni_{1.25}Fe_{1.75}(PO_4)_3$, projected along the *a* axis. $NiO_6$ and $FeO_6$ (8g) octahedra are grey, c) The crystal structure of $Na_{1.25}Ni_{1.25}Fe_{1.75}(PO_4)_3$, projected along the *c* axis. d) The crystal structure of $Na_{1.25}Ni_{1.25}Fe_{1.75}(PO_4)_3$, projected along the *b* axis. $NiO_6$ and $FeO_6$ (8g) octahedra are grey, $FeO_6$ (4e) octahedra are brown $NiO_6$ and $FeO_6$ (8g) octahedra are grey, $FeO_6$ (4e) octahedra are brown, $PO_4$ tetrahedra are violet, and Na atoms are yellow. (For interpretation of the references to colour in this figure legend, the reader is referred to the Web version of this article.)

**Table 2**
Experimental details for the Rietveld refinement of NNFP.

| | |
|---|---|
| Number of reflexions | 266 |
| Refined Parameters | 43 |
| Positional | 14 |
| Population | 2 |
| Thermal | 4 |
| Cell parameters | 3 |
| Profile | 4 |
| Background | 7 |
| Crystallite size, zero point, sample displacement, LP factor, roughness, absorption, thickness, scale factor | 9 |
| *Space group* | *Imma* (no 74) |
| *a* (Å) | 10.473(2) |
| *b* (Å) | 13.176(3) |
| *c* (Å) | 6.473(1) |
| $R_p$ (%) | 3.32 |
| $R_{wp\ (\%)}$ | 4.65 |
| $R_{exp.}$ (%) | 0.53 |
| S (GooF) | 8.71 |
| $R_{Bragg}$ (%) | 2.64 |

**Table 3**
Positional (*x,y,z*), isotropic thermal (*B*) and site occupancy (*N*) parameters for NNFP.

| Site | Wyckoff | *X* | *Y* | *Z* | *B* (Å$^2$) | *N* |
|---|---|---|---|---|---|---|
| Na1 | 4e | 0 | ¾ | 0.599(2) | 1.0 | 0.61(2) |
| Na2 | 4b | 0 | ½ | ½ | 1.0 | 0.66(2) |
| Ni1/Fe1 | 8g | ¼ | 0.6347(3) | ¼ | 4.1(4) | 0.64/0.36 |
| Fe2 | 4a | ½ | ½ | ½ | 3.8(5) | 1.00 |
| P1 | 8g | ¼ | 0.4319(5) | ¼ | 2.7(4) | 1.0 |
| P2 | 4e | 0 | ¾ | 0.069(1) | 2.7(4) | 1.0 |
| O1 | 16j | 0.2833(6) | 0.3659(7) | 0.0707(9) | 3.2(4) | 1.0 |
| O2 | 16j | 0.1435(7) | 0.5102(5) | 0.215(1) | 3.2(4) | 1.0 |
| O3 | 8h | 0 | 0.6436(9) | 0.962(2) | 3.2(4) | 1.0 |
| O4 | 8i | 0.1203(9) | ¾ | 0.231(2) | 3.2(4) | 1.0 |

**Table 4**
Interatomic distances (Å) for NNFP.

| | | | |
|---|---|---|---|
| Na1-O3 (x2) | 2.671(19) | Ni1/Fe1-O4 (x2) | 2.042(7) |
| Na1-O1 (x2) | 2.742(8) | Ni1/Fe1-O2 (x2) | 2.095(8) |
| Na1-O4 (x2) | 2.695(14) | Ni1/Fe1-O1 (x2) | 2.105(13) |
| **Mean** | 2.703 | **Mean** | 2.081 |
| Na2-O2 (4) | 2.380(13) | Fe2-O2 (x4) | 2.049(11) |
| Na2-O1 (4) | 2.913(8) | Fe2-O3 (x2) | 2.039(13) |
| **Mean** | 2.647 | **Mean** | 2.044 |
| P1-O1(x2) | 1.492(13) | P2-O3 (x2) | 1.447(16) |
| P1-O2(x2) | 1.459(10) | P2-O4 (x2) | 1.639(14) |
| **Mean** | 1.476 | **Mean** | 1.543 |

(Table 5). There is no increase of hysteresis loop during adsorption-desorption of $N_2$ (Fig. S1). This confirms that NNFP particles are uniform and non porous, in agreement with the size distribution and the morphology of the particles observed by SEM and TEM. The rather high surface area of 14 $m^2g^{-1}$ is consistent with the submicrometer size of the particles.

### 3.6. Electrochemical properties

#### 3.6.1. $Na_{1.25}Ni_{1.25}Fe_{1.75}(PO_4)_3$ as anode material

Fig. 5a shows cyclic voltammograms (CV) of the Li//NNFP sample in the voltage range of 0.03–3.6 V at 0.5 mV/s. The first scan begins from open circuit potential at 2.8 V down to 0.01 V. The voltammetric response of the first cycle is noticeably different from the other cycles. The first discharge curve show two mean peaks at around 1.4 and 1 V, that could correspond to the $Fe^{2+/0}$, $Ni^{2+/0}$ redox couples, respectively.

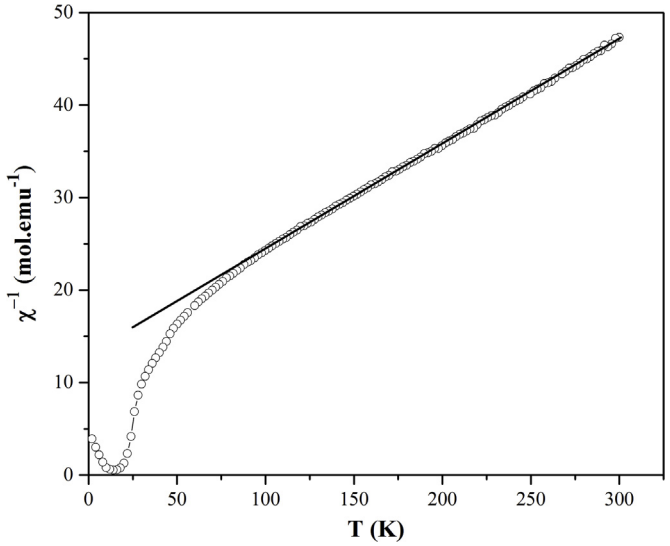


**Fig. 3.** Temperature dependence of the inverse magnetic susceptibility of $Na_{1.25}Ni_{1.25}Fe_{1.75}(PO_4)_3$.

This indicates that the reaction occurring at the first discharge is irreversible, which corresponds to the decomposition of phosphate upon initial reaction with Li. During the first charge, a broad peak around 2.8 V and small peak at 3.4 V were detected, that could be tentatively attributed to the partial oxidation to $Fe^0$ and $Ni^0$. The second discharge shows a principal peak at around 1.56 V. The typical voltage profiles for lithium insertion/deinsertion in NNFP were obtained in galvanostatic regime with a 40 mA $g^{-1}$ current density and the potential window 0.03–3.5 V vs. $Li/Li^+$ (Fig. 5b). The initial step is the discharge of the battery until 0.03V. At the beginning of the first discharge, there is a small voltage plateau at about 3 V and then the voltage quickly drops to about 1.6 V. This potential range corresponds to the reduction of $Fe^{3+}$ into $Fe^{2+}$ in NNFP. Then, there is a small plateau between 1.6 V and 1.4 V. A more extended plateau between 1.4 V and 1.25V could be attributed to the reduction of $Fe^{2+}$ and $Ni^{2+}$ into $Fe^0$ and $Ni^0$, respectively. Such a reduction of $M^{2+}$ to $M^0$ has been already identified in oxyphosphates $M_{0.5}TiOPO_4$ (M: Ni, Co and Fe) [33–37]. The capacity

**Table 5**
BET (Brunauer–Emmett–Teller) surface area and pore volumes determined by Nitrogen sorption for NNFP sample.

| Sample | BET Surface Area ($m^2g^{-1}$) | Total pore volume ($cm^3g^{-1}$) | Pore Diameter (nm) |
|---|---|---|---|
| NNFP | 13.8 | 0.022 | 6.4 |

(431.2 mAh $g^{-1}$) measured at 1.25V represents the total capacities for these mechanisms and is quite close to the theoretical capacity (428 mAh $g^{-1}$) evaluated by considering the intercalation of 7.5 $Li^+$ ions per f.u., which corresponds to the total reduction of $Fe^{3+}$ and $Ni^{2+}$ into $Fe^0$ and $Ni^0$, respectively. This may suggest a conversion reaction during the first discharge [38]. However, the material delivers an additional capacity of about 755 mAh $g^{-1}$ for a total capacity 1186 mAh $g^{-1}$ for the first discharge. There is a strong irreversibility at the first discharge since the reversible capacity is about 670 mAh $g^{-1}$. The origin of this additional capacity is still unclear but should reflect the combination of different mechanisms. The electrolyte reduction at the electrode/electrolyte interface could explain the plateau around 0.9 V while side reactions at the interface between the remaining electrode particles and the electrolyte could be a possible mechanism at lower potentials both leading to the formation of surface electrolyte interphases (SEI) [24,38]. Because the first discharge is not fully understood, it is difficult to propose reaction mechanisms for the following charge/discharge cycles that clearly differ from the first discharge. A more detailed analysis requires operando techniques and is out of the scope of the present work.

Rate capability is another important electrochemical parameter because it informs about electron and ion conductivity during charge/discharge processes at different current densities. The rate capability of the NNFP/Li half-cells has been studied in two potential ranges: 0.03–3.0 V and 0.03–3.5 V for comparison (Fig. 6a). NNFP anode material delivers high specific capacities of 442, 292, 212 and 130 mAh $g^{-1}$ in the 0.03–3.0 V voltage window and 545, 335, 241 and 141 mAh $g^{-1}$ in the 0.03–3.5 V voltage window at the current densities of 50, 100, 200, and 500 mA $g^{-1}$, respectively. The obtained specific capacity as a function of the discharge current density is plotted in Fig. 6b. Furthermore, the NNFP electrode possesses excellent capacity retention (Fig. 6c). After continuous cycling for 350 cycles at a current density of

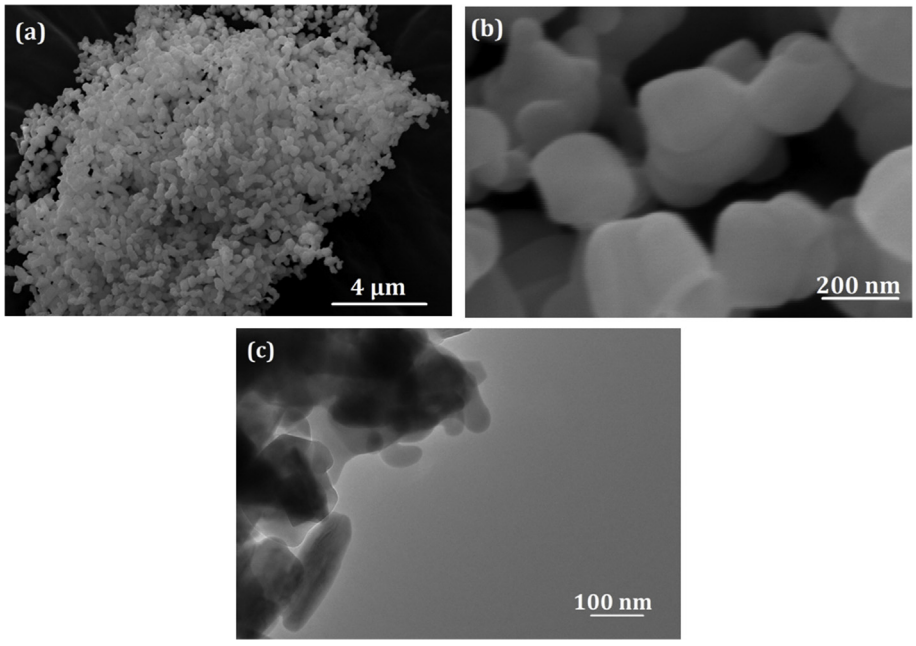


**Fig. 4.** (a, b) SEM and (c) TEM micrographs of $Na_{1.25}Ni_{1.25}Fe_{1.75}(PO_4)_3$.

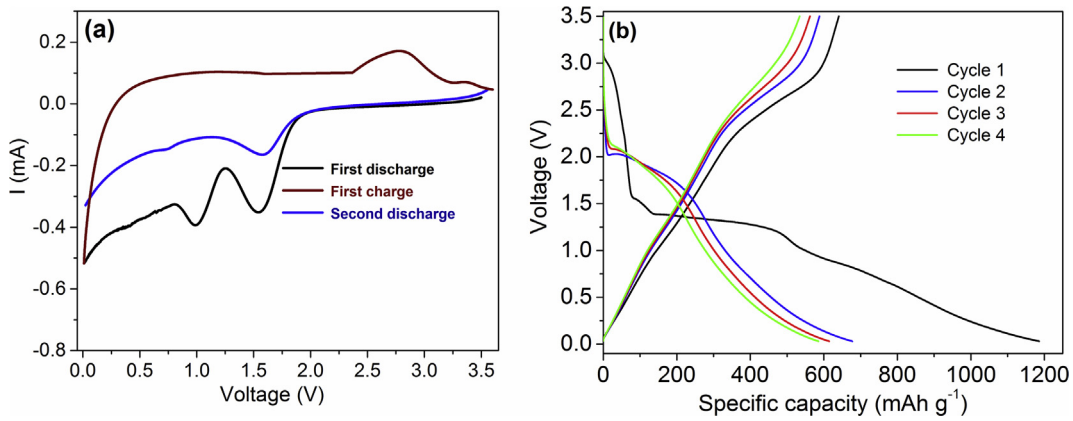


**Fig. 5.** (a) Cyclic voltammetry analysis of NNFP at 0.5 mV $s^{-1}$ scan rate in 0.03-3.6V voltage range, (b) typical charge-discharge curves at 40 mAh.$g^{-1}$ (~C/10) current density for $Na_{1.25}Ni_{1.25}Fe_{1.75}(PO_4)_3$. The potential voltage window is 0.03–3.5 V vs. $Li^+/Li^0$.

50, 200 and 400 mA $g^{-1}$, reversible average discharge capacity of about 450, 220 and 138 mAh $g^{-1}$ are retained in 0.03–3.0 V voltage window. Fig. S2 illustrates the good electrochemical performance of NNFP as anode material for lithium-ion batteries thanks to its good cycling stability and high coulombic at a current density of 200 mA$g^{-1}$. The coulombic efficiency varies between 99.6% and 100%, indicating excellent cycling stability and reversibility of intercalation/deintercalation processes. These results show that the NNFP nanoparticles as negative electrode exhibit excellent high-rate capability compared to graphite commonly used in commercial batteries as negative electrode in lithium.

### 3.6.2. $Na_{1.25}Ni_{1.25}Fe_{1.75}(PO_4)_3$ as cathode material

The electrochemical properties of the NNFP as cathode material were evaluated at room temperature in half-cells with lithium metal as counter electrode in the potential window: 1.5–4.5 V vs. Li/$Li^+$. Cyclic voltammograms (CV) were obtained at a scan rate of 0.5 mV $s^{-1}$ (Fig. 7a) and the galvanostatic voltage profile with a current density of 5 mA $g^{-1}$ (Fig. 7b). The first step of the galvanostatic test is a charge up to 4.5 V showing an almost negligible capacity (10 mAh $g^{-1}$). The voltage profile of the first discharge is similar to that obtained at the beginning of the full discharge shown in Fig. 5b. The plateaus at 3.2V and 1.6 V are confirmed by CV reduction peaks and mainly reflect the reduction of $Fe^{3+}$ into $Fe^{2+}$ and the beginning of the possible reduction of $Ni^{2+}$, respectively. The observed discharge capacity of 126 mAh $g^{-1}$ corresponds to intercalation of about 2.28 $Li^+$ per f.u. in the electrode material. This capacity is slightly higher than that expected for the insertion of 1.75 $Li^+$ per f.u. corresponding to the only reduction of $Fe^{3+}$ into $Fe^{2+}$ (96.8 mAh $g^{-1}$) confirming the additional capacity could be due to the partial reduction of $Ni^{2+}$ or to the structural changes during the first discharge. Indeed, the first discharge voltage curve is different from the other following cycles showing high polarization, which confirms that the insertion mechanism is complex and different for the first lithiation. When NNFP is used as anode material in the voltage range 0.03–3.5 V, the material delivers a specific capacity of 1186 mAh g−1, which is almost three times its theoretical capacity (428 mAh g-1) expected by the reduction of $Fe^{3+}$ and $Ni^{2+}$ into $Fe^0$ and $Ni^0$, respectively. This is a clear indication of the destruction of the structure of the pristine material and its transformation to other chemical species (alkali phosphates, metal particles, etc.). The possible active redox couples involved in the electrochemical reactions of NNFP as anode material with Li are $Fe^{3+}/Fe^{2+}$, $Fe^{2+}/Fe^0$ and $Ni^{2+}/Ni^0$. This

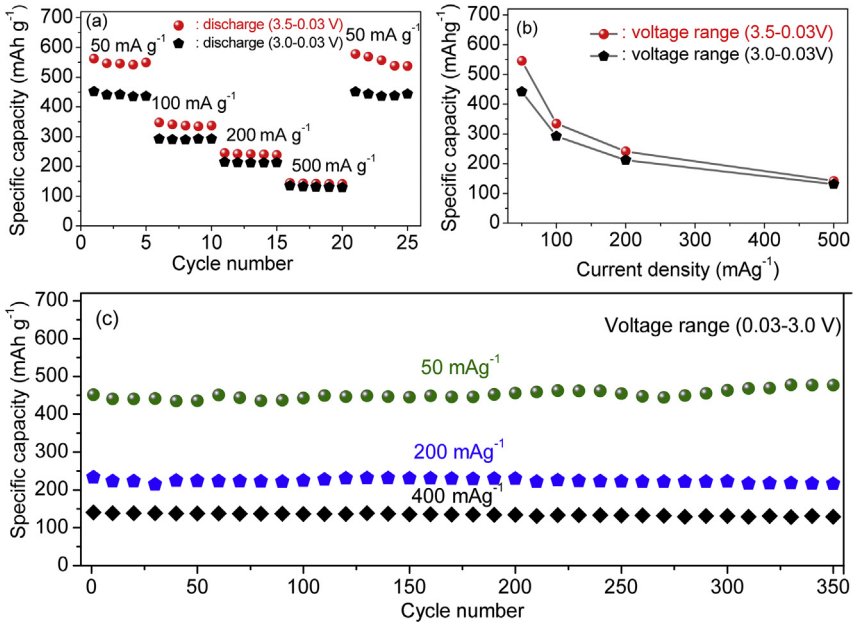


**Fig. 6.** (a) rate capability at different current densities in 0.03–3.5 V and 0.03–3.0 V voltage windows, (b) evolution of discharge capacity as a function of discharge rate; c) cycling performance at a current densities of 50, 200 and 400 mA $g^{-1}$.

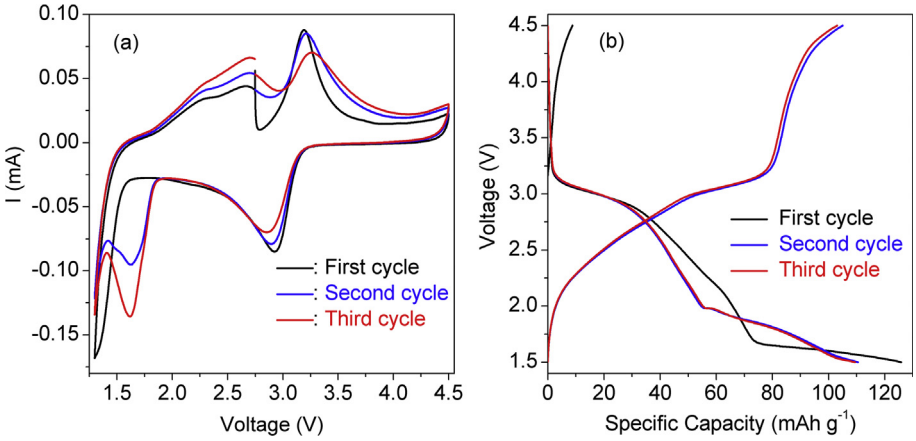


**Fig. 7.** Electrochemical evaluation of $Na_{1.25}Ni_{1.25}Fe_{1.75}(PO_4)_3$ particles as cathode material for lithium-ion batteries: (a) Cyclic voltammetry analysis and (b) discharge–charge *vs* voltage profiles of the first 3 cycles at a current density of 5 m A.$g^{-1}$ in 1.5–4.5V voltage range.

can be related to conversion-type reaction mechanism which leads to the complete transformation of the NNFP pristine material. At low voltage, the reduction of the electrolyte and the formation of solid electrolyte interphase (SEI) also occurred, which leads to high irreversibility for the first cycle. Indeed, it has been shown that electrolyte species decomposition on the anode surface contribute to the first cycle capacity loss [39]. As shown by the voltage profile of the first charge, the mechanism is not fully reversible but the capacity loss is small (12%). There is neither low voltage plateau for the first charge nor the corresponding CV peak, in line with the irreversibility of the reduction $Ni^{2+}$ to $Ni^0$. The shape of the voltage curve below 80 mAh $g^{-1}$ shows some similarities with that of the first discharge. This shows the reversibility of the $Fe^{3+} \leftrightarrow Fe^{2+}$ transformation but the existence of different oxidation peaks at 2.25, 2.72 and 3.20 V suggests a more complex and multi-step reaction mechanism. The potential profile of the second discharge differs from that of the first discharge in the second part of the process, in line with the existence of the CV reduction peak at 1.6 V. This is also an indication for a multi-step mechanism but different from the first charge. Then, the following cycles have the same voltage and CV profiles as the cycle formed by the first charge and the second discharge showing the mechanism is reversible only after the first discharge.

Fig. 8a shows the cycling performances of NNFP′ electrode material in the voltage window of 1.5–4.5 V at different current densities from 5 to 300 mA $g^{-1}$. The material delivers specific capacities of 126, 83, 70, and 45 mAh $g^{-1}$ at the current densities of 5, 50, 100, and 300 mA $g^{-1}$, respectively. Furthermore, it should be also indicated that the capacity was recovered when the current density is changed back to 5 mA $g^{-1}$, the reversible capacity reaches 145 mAh $g^{-1}$, confirming the good structural stability of NNFP material. This result demonstrates that the NNFP structure was not destroyed during the rate capability studies. Consequently, the drop of charge/discharge capacity on increasing the discharge rate was due to kinetic limitations of $Li^+$-insertion processes into the NNFP material. The specific capacity is reported as a function of the discharge current density in Fig. 8b. On continuous cycling for 100 cycles at a current density of 50 mA $g^{-1}$ (Fig. 8c), a reversible discharge capacity as high as 92 mAh $g^{-1}$ is retained, corresponding to 95% of the initial capacity. This shows that NNFP electrode also possesses very good rate capability and cyclic stability (Fig. 8a and c) as cathode materials.

We have summarized the comparison of the electrochemical performance of $\square_{0.75}Na_{1.25}Ni_{1.25}Fe_{1.75}(PO_4)$ nanoparticles obtained by

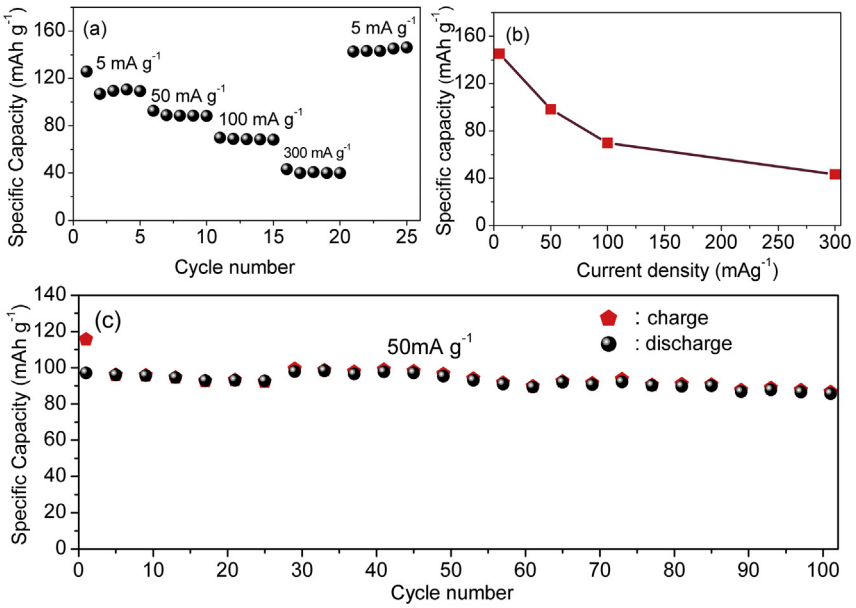


**Fig. 8.** Electrochemical evaluation of $Na_{1.25}Ni_{1.25}Fe_{1.75}(PO_4)_3$ particles as cathode material for lithium-ion batteries: (a) rate capability at different current densities between 1.5 and 4.5 V; (b) evolution of discharge capacity as a function of discharge rate; c) cycling performance at a current densities of 50 mA $g^{-1}$.

solvothermal synthesis and other related materials obtained by various synthesis methods such as solid state synthesis, sol-gel and hydrothermal synthesis route in Fig. S3. Fig. S4 shows the electrochemical performances of NNFP as anode and cathode materials for Na-ion batteries.

## 4. Conclusions

In this work, we have presented a study of $Na_{1.25}Ni_{1.25}Fe_{1.75}(PO_4)_3$ prepared for the first time by a facile solvothermal synthesis method that can be scaled up for industrial production. The synthesis strategy used here allowed us to obtain $Na_{1.25}Ni_{1.25}Fe_{1.75}(PO_4)_3$ nanoparticles with rather optimized morphology for application as electrode materials. This method first involves the synthesis of an intermediate precursor by a simple solvothermal method that is then transformed into $Na_{1.25}Ni_{1.25}Fe_{1.75}(PO_4)_3$ nanoparticles by a simple thermal annealing under air. The composition and the structure were accurately determined by combining $^{57}Fe$ Mössbauer spectroscopy, XRD Rietveld refinements and magnetic measurements. The material showed dual active voltage and exhibited interesting electrochemical performances as cathode and anode for Li-ion batteries in terms of specific capacity, rate capability and capacity retention. The potential profiles reflect multi-step insertion/deinsertion mechanisms that should be elucidated by operando characterization tools in order to have a better understanding of the synthesis-crystal structure-electrochemical performances relationships.

## Acknowledgements

The authors are grateful to University of Liege and F.R.S. - FNRS for equipment grants. Part of this work was supported by the Walloon Region under the “PE PlanMarshall2.vert” program (BATWAL – 1318146).C. Karegeya acknowledges the abroad study leave of the University of Rwanda. A. Mahmoud is grateful to the Walloon region for a Beware Fellowship Academia 2015-1, RESIBAT n° 1510399. The authors are grateful to Corine Reibel and Joris Vezzani for magnetic and BET measurements, respectively.

## Appendix A. Supplementary data

Supplementary data related to this article can be found at http://dx.doi.org/10.1016/j.jpowsour.2018.03.069.

## References

[1] P. Benedek, N. Wenzler, M. Yarema, V.C. Wood, Low temperature hydrothermal synthesis of battery grade lithium iron phosphate, RSC Adv. 7 (2017) 17763–17767.
[2] C. Masquelier, Laurence Croguennec, Polyanionic (phosphates, silicates, sulfates) frameworks as electrode materials for rechargeable Li (or Na) batteries, Chem. Rev. 113 (2013) 6552–6591.
[3] L. Shen, L. Yu, X.-Y. Yu, X. Zhang, X.W.D. Lou, Self-Templated formation of uniform $NiCo_2O_4$ hollow spheres with complex interior structures for lithium-ion batteries and supercapacitors, Angew. Chem. Int. Ed. 54 (2015) 1868–1872.
[4] T. Kim, E. Momin, J. Choi, K. Yuan, H. Zaidi, J. Kim, M. Park, N. Lee, M.T. McMahon, A. Quinones-Hinojosa, J.W.M. Bulte, T. Hyeon, A.A. Gilad, Mesoporous silica-coated hollow manganese oxide nanoparticles as positive T 1 contrast agents for labeling and MRI tracking of adipose-derived mesenchymal stem cells, J. Am. Chem. Soc. 133 (2011) 2955–2961.
[5] B. Wang, J.S. Chen, H.B. Wu, Z. Wang, X.W. Lou, Quasiemulsion-templated formation of α-$Fe_2O_3$ hollow spheres with enhanced lithium storage properties, J. Am. Chem. Soc. 133 (2011) 17146–17148.
[6] T. Kojima, T. Ishizu, T. Horiba, M. Yoshikawa, Development of lithium-ion battery for fuel cell hybrid electric vehicle application, J. Power Sources 189 (2009) 859–863.
[7] X.W.D. Lou, L.A. Archer, Z. Yang, Hollow micro-/nanostructures: synthesis and applications, Adv. Mater. 20 (2008) 3987–4019.
[8] X. Liu, J.-Q. Huang, Q. Zhang, X.-Y. Liu, H.-J. Peng, W. Zhu, F. Wei, N-Methyl-2-pyrrolidone-assisted solvothermal synthesis of nanosize orthorhombic lithium iron phosphate with improved Li-storage performance, J. Mater. Chem. 22 (2012) 18908–18914.
[9] C. Karegeya, A. Mahmoud, R. Cloots, B. Vertruyen, F. Boschini, Hydrothermal synthesis in presence of carbon black: particle-size reduction of iron hydroxyl phosphate hydrate for Li-ion battery, Electrochimica Acta, Electrochim. Acta 250 (2017) 49–55.
[10] K. Saravanan, P. Balaya, M.V. Reddy, B.V.R. Chowdari, J.J. Vittal, Morphology controlled synthesis of $LiFePO_4$/C nanoplates for Li-ion batteries, Energy Environ. Sci. 3 (2010) 457–463.
[11] H. Yang, X.-L. Wu, M.-H. Cao, Y.-G. Guo, Solvothermal synthesis of $LiFePO_4$ hierarchically dumbbell-like microstructures by nanoplate self-assembly and their application as a cathode material in lithium-ion batteries, J. Phys. Chem. C 113 (2009) 3345–3351.
[12] C. Karegeya, A. Mahmoud, B. Vertruyen, F. Hatert, R.P. Hermann, R. Cloots, F. Boschini, One-step hydrothermal synthesis and electrochemical performance of sodium-manganese-iron phosphate as cathode material for Li-ion batteries, J. Solid State Chem. 253 (2017) 389–397.
[13] S. Yang, X. Zhou, J. Zhang, Z. Liu, Morphology-controlled solvothermal synthesis of $LiFePO_4$ as a cathode material for lithium-ion batteries, J. Mater. Chem. 20 (2010) 8086–8091.
[14] Z.G. Lu, M.F. Lo, C.Y. Chung, Pulse laser deposition and electrochemical characterization of $LiFePO_4$-C composite thin films, J. Phys. Chem. C 112 (2008) 7069–7078.
[15] C. Karegeya, A. Mahmoud, B. Vertruyen, F. Hatert, R. Cloots, F. Boschini, Hydrothermal Self-assembly of Sodium Manganese Iron Phosphate Particles: Growth Mechanism and Electrochemical Performance in Lithium-ion Battery, Solid State Ionics 312 (2017) 88–96.
[16] A.V. Murugan, T. Muraliganth, A. Manthiram, Rapid microwave-solvothermal synthesis of phospho-olivine nanorods and their coating with a mixed conducting polymer for lithium ion batteries, Electrochem. Commun. 10 (2008) 903–906.
[17] A. Mahmoud, J.M. Amarilla, I. Saadoune, Effect of thermal treatment used in the sol–gel synthesis of $Li_4Ti_5O_{12}$ spinel on its electrochemical properties as anode for lithium ion batteries, Electrochim. Acta 163 (2015) 213–222.
[18] M. Gaberscek, R. Dominko, M. Bele, M. Remskar, D. Hanzel, J. Jamnik, Porous, carbon-decorated $LiFePO_4$ prepared by sol–gel method based on citric acid, Solid State Ionics 176 (2005) 1801–1805.
[19] C. Delacourt, P. Poizot, S. Levasseur, C. Masquelier, Size effects on carbon-free $LiFePO_4$ powders the key to superior energy density, Electrochem. Solid State Lett. 9 (2006) A352–A355.
[20] G. Arnold, J. Garche, R. Hemmer, S. Ströbele, C. Vogler, M. Wohlfahrt-Mehrens, Fine-particle lithium iron phosphate $LiFePO_4$ synthesized by a new low-cost aqueous precipitation technique, J. Power Sources 119 (2003) 247–251.
[21] Z. Wang, S. Su, C. Yu, Y. Chen, D. Xia, Synthesises, characterizations and electrochemical properties of spherical-like $LiFePO_4$ by hydrothermal method, J. Power Sources 184 (2008) 633–636.
[22] K. Dokko, S. Koizumi, K. Sharaishi, K. Kanamura, Electrochemical properties of $LiFePO_4$ prepared via hydrothermal route, J. Power Sources 165 (2007) 656–659.
[23] A. Mahmoud, J.M. Amarilla, K. Lasri, I. Saadoune, Influence of the synthesis method on the electrochemical properties of the $Li_4Ti_5O_{12}$ spinel in Li-half and Li-ion full-cells. A systematic comparison, Electrochim. Acta 93 (2013) 163–172.
[24] R. Essehli, I. Belharouak, H.B. Yahia, R. Chamoun, B. Orayech, B. El Bali, K. Bouziane, X.L. Zhou, Z. Zhou, α-$Na_2Ni_2Fe(PO_4)_3$: a dual positive/negative electrode material for sodium ion batteries, Dalton Trans. 44 (2015) 4526–4532.
[25] K. Saravanan, M.V. Reddy, P. Balaya, H. Gong, B.V.R. Chowdari, J.J. Vittal, Storage performance of $LiFePO_4$ nanoplates, J. Mater. Chem. 19 (2009) 605–610.
[26] C. Nan, J. Lu, C. Chen, Q. Peng, Y. Li, Solvothermal synthesis of lithium iron phosphate nanoplates, J. Mater. Chem. 21 (2011) 9994–9996.
[27] L. Samain, P. Amshoff, J.J. Biendicho, F. Tietz, A. Mahmoud, R.P. Hermann, S.Y. Istomin, J. Grins, G. Svensson, Crystal structure and high-temperature properties of the Ruddlesden–Popper phases $Sr_{3-x}Y_x(Fe_{1.25}Ni_{0.75})O_{7-\delta}$ ($0 \le x \le 0.75$), J. Solid State Chem. 227 (2015) 45–54.
[28] R.P. Hermann, V. Keppens, P. Bonville, G.S. Nolas, F. Grandjean, G.J. Long, H.M. Christen, B.C. Chakoumakos, B.C. Sales, D. Mandrus, Direct experimental evidence for atomic tunneling of europium in crystalline $Eu_8Ga_{16}Ge_{30}$, Phys. Rev. Lett. 97 (2006) 017401.
[29] R.D. Shannon, Revised effective ionic radii and systematic studies of interatomic distances in halides and chalcogenides, Acta Crystallogr. A. 32 (1976) 751–767.
[30] N. Kinomura, N. Matsui, N. Kumada, F. Muto, Synthesis and crystal structure of $NaV_3P_3O_{12}$: a stuffed structure of α-$CrPO_4$, J. Solid State Chem. 79 (1989) 232–237.
[31] M.B. Korzenski, J.W. Kolis, G.J. Long, Hydrothermal synthesis, structural characterization, and physical properties of a new mixed valence iron phosphate, $SrFe_3(PO_4)_3$, J. Solid State Chem. 147 (1999) 390–398.
[32] J.P. Attfield, A. t Sleight, A.K. Cheetham, Structure determination of α-$CrPO_4$ from powder synchrotron X-ray data, Nature 322 (1986) 620–622.
[33] I. Belharouak, K. Amine, New active titanium oxyphosphate material for lithium batteries, Electrochem. Commun. 7 (2005) 648–651.
[34] K. Lasri, I. Saadoune, Y. Bentaleb, D. Mikhailova, H. Ehrenberg, L. Häggström, K. Edström, Origin of the irreversible capacity of the $Fe_{0.5}TiOPO_4$ anode material, Solid State Ionics 224 (2012) 15–20.
[35] R. Essehli, B. El Bali, A. Faik, M. Naji, S. Benmokhtar, Y.R. Zhong, L.W. Su, Z. Zhou, J. Kim, K. Kang, M. Dusek, Iron titanium phosphates as high-specific-capacity electrode materials for lithium ion batteries, J. Alloy. Comp. 585 (2014) 434–441.
[36] R. Essehli, B. El Bali, A. Faik, S. Benmokhtar, B. Manoun, Y. Zhang, X.J. Zhang, Z. Zhou, H. Fuess, Structural changes upon lithium insertion in $Ni_{0.5}TiOPO_4$, J. Alloy. Comp. 530 (2012) 178–185.
[37] R. Essehli, I. Belharouak, H.B. Yahia, K. Maher, A. Abouimrane, B. Orayech, S. Calder, X.L. Zhou, Z. Zhou, Y.K. Sun, Alluaudite $Na_2Co_2Fe(PO_4)_3$ as an electroactive material for sodium ion batteries, Dalton Trans. 44 (2015) 7881–7886.
[38] K. Lasri, A. Mahmoud, I. Saadoune, M.T. Sougrati, L. Stievano, P.-E. Lippens, R.P. Hermann, H. Ehrenberg, Toward understanding the lithiation/delithiation process in $Fe_{0.5}TiOPO_4$/C electrode material for lithium-ion batteries, Sol. Energy Mater. Sol. Cells 148 (2016) 11–19.
[39] A. Mahmoud, M. Chamas, P.-E. Lippens, Electrochemical impedance study of the solid electrolyte interphase in $MnSn_2$ based anode for Li-ion batteries, Electrochim. Acta 184 (2015) 387–391.